ELSEVIER

Journal of Nuclear Materials 273 (1999) 294–301

journal of nuclear materials

www.elsevier.nl/locate/jnucmat

Determination of the solidus temperatures of Zircaloy-4/oxygen alloys

P.J. Hayward *, I.M. George

Atomic Energy of Canada Limited, Whiteshell Laboratories, Pinawa, Manitoba, Canada R0E 1L0

Received 19 November 1998; accepted 8 February 1999

Abstract

Solidus temperatures have been measured for a series of Zircaloy-4/oxygen alloys, ranging from as-received (nominally O-free) Zircaloy to O-saturated Zircaloy. The data were obtained using a pyrometer-based differential thermal analysis technique. The results are in broad agreement with generally accepted values for the binary Zr–O system, except that there is a slight reduction in the solidus temperatures, caused by the presence of Sn, Fe and Cr in the pseudo-binary Zircaloy–O system. The solidus for O-saturated Zircaloy occurs at 2318 ± 20 K, which is 145–185 K higher than the value assumed in many fuel-safety assessments.

1. Introduction

The ability of Zircaloy-4 (Zry) cladding to accommodate significant amounts (~29 at.% or ~7 wt% at room temperature) of oxygen in solid solution is well known. There are, however, no published data for the solidus and liquidus temperatures of Zry(O) alloys. The solidus temperatures are of particular importance for interpreting and modeling core-melt progression phenomena, because formation of a liquid phase would cause a significant increase in the rate of subsequent fuel/cladding reaction. For this reason, a subroutine relating the Zry/O solidus temperature to the cladding oxygen content is incorporated in many severe fuel damage (SFD) codes.

One reason for the lack of Zry(O) melting data is the practical difficulty in performing the measurements, caused by the high chemical reactivity of molten Zr alloys towards most refractory container materials. Molten Zry will alloy with all refractory metals, and will react with carbide, nitride and boride ceramics to form ZrC, ZrN and ZrB_2, respectively. It also reacts with most oxide ceramics, e.g. thoria, forming mixed-cation ceramics of the type (Th, Zr)O_{2-x}. Stabilised ZrO_2 is dissolved by molten Zry to form α-Zr(O) and ZrO_{2-x} in quantities dictated by the starting-material amounts. Although yttria does not dissolve in molten Zry, it nevertheless turns black, suggesting that the oxide becomes hypostoichiometric from O-diffusion into the melt.

In the absence of direct measurements with Zry/O alloys, many SFD safety assessments use melting data for Zr–O to simulate those of Zry–O. This approach ignores the influence of the Zry alloy elements (~1.5% Sn, 0.2% Fe, 0.1% Cr) on melting properties. The low concentration of these elements is still sufficient, however, to reduce the melting point of pure Zr from 2128 K [1] to a value of ~2033 K for O-free Zry. It would, therefore, be reasonable to expect similar reductions in the solidus, liquidus and peritectic reaction temperatures of Zry(O) alloys, compared to those of Zr(O), provided that the alloy elements remain in solid solution during Zry oxygenation.

A further complication is the lack of general agreement on solidus and liquidus temperatures in the Zr–O system. For example, published values for the solidus temperature of O-saturated Zr vary between 2173 [2,3], 2273 [4] and 2338 K [5]. The MATPRO library [6] lists a value of 2173 K for the solidus temperature of O-saturated Zry, presumably based on the earlier Zr–O results [2,3]. Other proprietary data compilations quote solidus

* Corresponding author. Tel.: +1-204 753 8338; fax: +1-204-753 2455; e-mail: haywardp@mb.sympatico.ca.

0022-3115/99/$ – see front matter
PII: S0022-3115(99)00050-1

temperatures for O-saturated Zry ranging from 2133 to 2338 K.

To fill this gap in the SFD data base, we have performed measurements of the solidus temperatures for a series of Zry(O) alloys, ranging from as-received (nominally O-free) Zry to O-saturated Zry. The data were obtained using a pyrometer-based differential thermal analysis (DTA) technique, referred to below as PDTA. For reasons discussed in Section 2.2, the PDTA technique did not allow the liquidus temperatures to be accurately determined. As noted above, however, the solidus temperatures are more significant for SFD modeling.

2. General aspects of pyrometric DTA measurements

The PDTA technique is similar in principle to conventional (thermocouple-based) DTA, and is used to measure the temperature at which a first order transition occurs during heating or cooling of a material under investigation. First order transitions are indicated by a discontinuous change in the Gibbs free energy function, and include melting, freezing and crystallographic transitions.

2.1. Measurement procedure

The PDTA technique involves heating or cooling a specimen of the material under investigation, together with an inert black-body material, at a fixed rate, while simultaneously recording the specimen and black-body temperatures with dual-wavelength pyrometers. The temperature difference between the specimen and the black-body cavity (ΔT_{s-bb}) is plotted against the black-body cavity temperature (T_{bb}). A first order transition is shown as peak in the trace, produced by the exothermic or endothermic reaction and/or a change in emissivity. As with conventional DTA, the technique works best when the trace does not contain multiple peaks from several closely spaced transitions. A typical procedure is as follows.

The specimen under investigation is placed on top of, or within, a black-body material, such as graphite or silicon carbide. Alternatively, the specimen may be located in a thin-walled ceramic crucible on top of a block of a refractory material (e.g. Mo, Ta or W) that contains a black-body cavity. The specimen/black-body assembly is positioned in the hot zone of a tungsten resistance furnace, with temperature control being provided by a Type C thermocouple coupled to a programmable controller. A dual wavelength pyrometer is focused on the specimen through a silica-glass window in the furnace roof. A second dual wavelength pyrometer is focused on the black body through a second window in the furnace sidewall, with the pyrometer emittance-ratio slope (*E*-slope) adjusted to the setting appropriate for a black body. The outputs from both pyrometers are recorded with a computer-based data acquisition system.

The furnace is initially evacuated and back-filled with ultra-high-purity (UHP) argon. The specimen is then heated to a temperature at the bottom end of the range in which measurements are to be made, and held at this temperature for a short time (1–2 min) to allow the specimen and black body temperatures to reach equilibrium. After this time, an empirical correction for specimen emissivity is made by adjusting the *E*-slope potentiometer of the specimen pyrometer to bring the recorded temperature into agreement with the temperature measured by the black-body pyrometer. This adjustment is based on the assumption that the specimen and black-body are at the same temperature.

The furnace is then programmed to heat each specimen/black-body assembly over the desired temperature range at a fixed ramp rate, usually in the range 30–60 K/min. The specimen and black-body temperatures are simultaneously recorded during heating, and subsequently plotted as ΔT_{s-bb} vs T_{bb}. The transition temperature is determined from the plot by the procedure described in Section 2.2.

The PDTA method has two main advantages over thermocouple-based DTA. A wider range of heating or cooling rates is possible because there is no thermal lag between the specimen surface and the sensing device. Furthermore, measurements can be made at much higher temperatures than would be possible with thermocouples. On the other hand, any changes in specimen emissivity will produce errors in the pyrometer measurements. These errors are minimised, however, by using dual wavelength pyrometers and a black body as the reference specimen.

2.2. Interpretation of results

The quantity of heat required to convert a material from solid to liquid (the heat of fusion) causes a thermal arrest in the plot of specimen temperature versus time, giving rise to an endothermic peak in the ΔT_{s-bb} vs T_{bb} plot. A material that melts congruently (i.e. forms a liquid of the same composition), such as an element, a fixed-stoichiometry compound or a eutectic composition, gives a sharp endothermic peak because the entire heat of fusion is absorbed at one temperature. For example, in Fig. 1(a), which shows a sketch of part of the Zr–O binary phase diagram [7], the melting of O-free Zr occurs at T_m. A schematic DTA trace for O-free Zr is illustrated in Fig. 1(b), showing the endothermic peak produced by melting. The melting point is given by the point where the trace departs from the baseline to form the endothermic peak, and is referred to as the peak-onset temperature. The specimen melting temperature (T_m) is given by $\Delta T_{s-bb} + T_{bb}$.

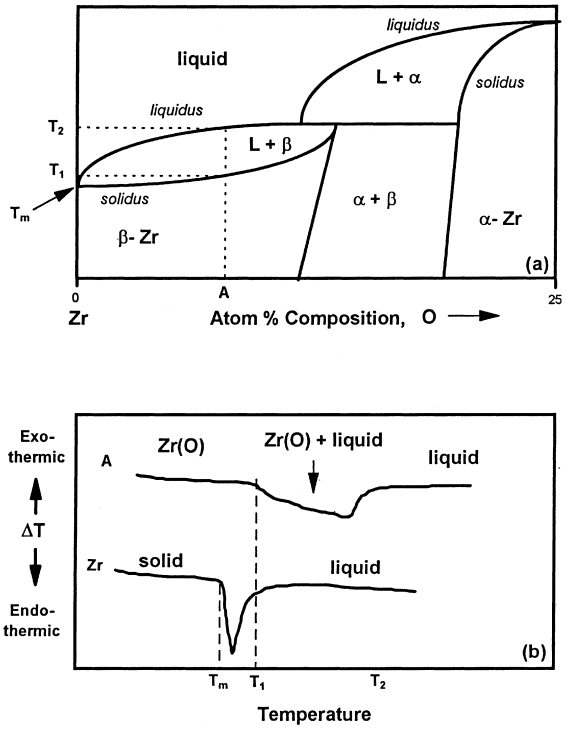

Fig. 1. Use of PDTA for determination of solidus temperatures: (a) sketch of part of the Zr–O system, showing liquidus and solidus lines; (b) schematic PDTA traces for Zr and for composition A during heating.

In practice, the temperature of the specimen interior will always lag behind that of the surface during heating, causing the peak to widen and to return to the baseline only after the entire specimen has melted. Thus, with a large specimen or high heating rate, the increased thermal lag will produce a broader peak of lower amplitude. It follows that the peak width and the temperature at the peak maximum are functions of specimen size and thermal conductivity, and have no fundamental meaning. The peak-onset temperature, however, remains unchanged, although the point at which the trace departs from the baseline becomes progressively more difficult to determine as the peak becomes broader.

In the case of a material that melts incongruently (i.e. forms a liquid of differing composition), melting occurs over a temperature range bounded by the solidus and liquidus lines, as illustrated in Fig. 1(a) for the Zr–O system. Thus, the heat of fusion is, in effect, spread out over this temperature range. Consequently, the endothermic DTA peak during heating becomes broader and shallower, making the peak-onset temperature harder to identify. These features are shown for composition A in Fig. 1(b). The DTA trace returns to the baseline when the material is fully liquid. However, because the peak width and amplitude are also influenced by thermal lag effects, only the solidus temperature can be precisely determined from the trace.

3. Experimental

3.1. Preparation of Zry/oxygen alloy specimens

The Zry(O) specimens were prepared from 2.5 mm thick slices cut from 6.35 mm diameter Teledyne Wah Chang Zircaloy-4 rod. The manufacturer's ingot analyses gave a mean composition (wt% $\pm 2\sigma$) as follows: Sn, 1.41 ± 0.09; Fe, 0.22 ± 0.01; Cr, 0.11 ± 0.01; O, 0.13 ± 0.04; Zr, balance. Each slice was individually oxidized to a target O content by heating in a thermobalance to 1673 K under an atmosphere of flowing Ar/1% O_2, using an yttria disc to support the specimen during oxidation. When the desired weight gain had been achieved, the atmosphere was switched to flowing UHP argon, and the specimen was held at 1673 K for up to 4 h to allow partial homogenization by O diffusion. Oxygen contents were calculated from the final weight gains of the cooled specimens, assuming an initial 0.13 wt% O content before oxidation.

To complete the homogenization process, the specimens were then re-annealed in yttria crucibles at 1923 K for 4 h, using a tungsten resistance furnace and an atmosphere of flowing UHP argon. This heat-treatment was selected on the basis of O-diffusion calculations, using Fick's law solutions given in Ref. [8] and O-diffusion coefficients for α-Zr(O), β-Zr and ZrO_2 obtained from the FROM.SFD/Mk2 code [9]. The annealed specimens were subsequently used for the PDTA measurements.

A parallel set of Zry(O) control specimens, spanning the entire range of desired O contents, was also prepared by identical methods to confirm that the oxidation and annealing procedures had produced suitably homogeneous specimens. The cooled specimens were sectioned along the cylinder-axis plane. One half of each specimen was polished to a 1 μm finish and then etched for 5–10 s in a 47% HNO_3, 47% lactic acid, 6% HF acid mixture to enhance topographical relief. The etched specimens were examined by optical microscopy and by scanning electron microscopy (SEM). Some energy dispersive X-ray (EDX) analyses were also performed on local regions within each specimen. The remaining half was dissolved in a HNO_3/HF acid solution and analyzed for Zr, Sn, Fe and Cr by inductively coupled plasma (ICP) emission spectrometry to check for loss of volatile elements during annealing.

3.2. PDTA measurements

The procedure was broadly similar to that used for previous measurements of the β/β + γ eutectoid

isotherm temperature in ZrO_{2-x} [10]. Several changes to the specimen/black-body configuration were made, however, to minimise any high temperature reaction between the Zry(O) alloy charges and their containers, and also to remove traces of residual air from the system.

Each Zry(O) specimen was contained in a crucible machined from a 13 mm side cube of high density graphite. The crucible cavity was produced by drilling an 8 mm diameter hole to a depth of ~8 mm, with the conical cavity bottom (formed by the drill tip) having an angle of ~120°. The 6.35 mm diameter specimen was placed in the cavity with the orientation shown in Fig. 2, a schematic diagram of the test assembly. Thus, the specimen/crucible contact during heating was restricted to the bottom circumferential edge of the specimen, thereby minimising any possibility for diffusion-based interaction prior to melting of the Zry(O) charge.

The Zr–C binary phase diagram [1] shows no solubility of C in Zr below 2078 K and only limited solubility at higher temperatures. The only compound formed in this system is ZrC, which, with a melting temperature of >3800 K, would remain solid during the PDTA measurements. Hence, no significant Zr/C interaction during heating was anticipated using this crucible/specimen design.

The graphite crucible and alloy charge were placed on top of an upturned thin-walled molybdenum crucible, which provided thermal insulation from the furnace stage and brought the square side of the graphite crucible into the line of sight of the side pyrometer. A similar pyrometer was focussed on the Zry(O) specimen through a silica-glass window in the furnace roof.

The furnace was initially evacuated to $\leqslant 10^{-5}$ Torr, using an oil-diffusion pump with a backup rotary pump, followed by heating to 773 K with the diffusion pump still running to thoroughly de-gas the system. The furnace was then back-filled with UHP argon that had been passed through an oxygen-scavenging cartridge to reduce oxygen impurities to <1 ppm. In later experiments

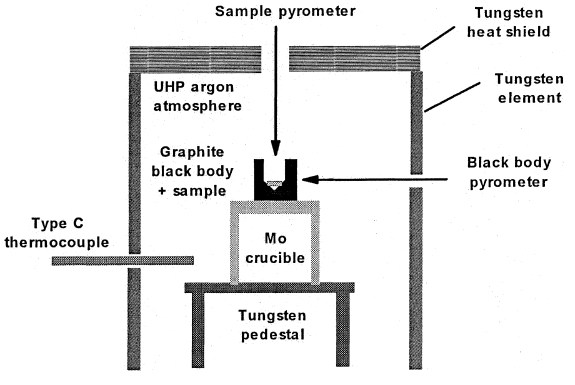

Fig. 2. Schematic diagram of PDTA specimen configuration.

with Zry(O) specimens containing <17 at.% O, the evacuation/back-filling procedure was performed three times at 1023 K to minimise any trace quantities of air and water vapour remaining in the system. After the final back-filling, a UHP argon flow of ~16 ml s^{-1} was maintained through the furnace chamber.

Each PDTA run was performed by heating the specimen rapidly to 1973 K, holding at this temperature for ~1 min to allow the specimen and black-body temperatures to reach equilibrium. The isothermal heating time was kept as short as possible to minimise any Zry/C interaction. After this time, the *E*-slope potentiometer of the specimen pyrometer was adjusted to bring the measured temperature into agreement with the black-body temperature, and the data acquisition system was turned on. The specimen temperature was then raised at a rate of 1 K/s, while the pyrometer readings were recorded at 1 s intervals. The run was terminated when the specimen temperature had reached ~150 K beyond the expected solidus temperature.

During most of the runs, the specimen was simultaneously observed through the upper pyrometer sighting lens. In this way, it was possible to identify the precise moment at which the specimen started to melt. The observations provided a useful check on the PDTA results, and were essential for correct interpretation of several of the more complex PDTA traces, as discussed below.

The PDTA traces from experiments with specimens of relatively high O contents (>17 at.%, i.e. lying in the α-Zr(O) field) generally gave uncomplicated traces and broad endothermic peaks. However, the traces from specimens with lower O contents (i.e. lying in the β-Zr(O) or [α-Zr(O) + β-Zr(O)] fields) often exhibited a series of endothermic and exothermic peaks. It was impossible to ascertain from the trace which of these peaks corresponded to the onset of melting. In these cases, the parallel observations through the pyrometer sighting lens allowed the PDTA peaks to be individually correlated with the following sequence of phenomena during heating:

1. for specimens with O contents of ~10–17 at.%, transformation of coexisting α-Zr(O) + β-Zr(O) to β-Zr(O), producing an endothermic peak;
2. rapid grain growth as the melting point was approached, also giving a change in specimen emissivity and producing an exothermic 'hump' or peak;
3. initial melting of the specimen, with the molten phase running down the specimen walls to leave the remaining solid specimen exposed. This phenomenon typically produced a series of endothermic peaks, with the first peak representing the onset of melting and
4. final melting, with the specimen forming a concave pool in the bottom of the crucible, causing a large change in specimen emissivity and an apparent large exothermic peak.

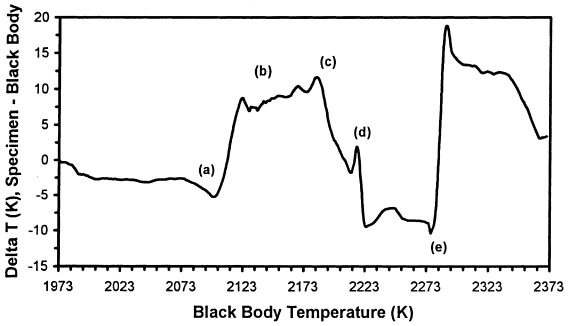

Fig. 3. PDTA trace for Zry/10.4 at.% O specimen showing sequence of events during heating: (a) transformation of [α-Zr(O) + β-Zr(O)] to β-Zr(O), producing an endothermic peak; (b) rapid grain growth as the melting point was approached, releasing heat and also causing an emissivity change; (c) initial melting, with the molten phase running down the specimen walls to leave the remaining solid specimen exposed; (d) melting of underlying material and (e) final melting and relocation to the bottom of the crucible, producing a sudden change in emissivity and a large exothermic peak.

Fig. 3 shows a typical trace for a Zry/10.4 at.% alloy, with the individual reaction stages identified.

In most cases, therefore, it was possible to identify which endothermic peak in a PDTA trace was caused by the onset of melting. The technique did not allow the liquidus temperatures (stage (iv) in the above sequence) to be measured, however, because of the significant change in specimen emissivity once melting had commenced. Consequently, only the solidus temperatures are reported below.

3.3. Temperature calibration

Both pyrometers used in this study had been factory calibrated using a black-body standard, with the calibration accuracy and repeatability being ±16 and ±5 K, respectively. Initial attempts were made to calibrate the PDTA system by measuring the melting point of Zr crystal bar specimens. These attempts failed because of very rapid and extensive grain growth just prior to melting, which produced an exothermic peak that completely obscured the subsequent endothermic peak caused by melting.

The system was, therefore, calibrated by repeated melting point determinations with a pure Pt specimen, contained in a thin-walled Y_2O_3 crucible on top of the graphite black body to avoid Pt–C reaction. Thermal cycling of the specimen within the temperature range 1973–2173 K gave peak-onset temperatures during heating of 2035, 2031, 2048 and 2033 K. The mean value $\pm 2\sigma$ of 2037 ± 15 K for the Pt melting point is in good agreement with the literature value of 2042 K [1].

Based on these calibration results, it seems reasonable to take the ±16 K calibration accuracy of the pyrometers as the maximum error in temperature measurement, ε_1. There are two further sources of uncertainty: (i) ε_2, the error in determining the point of departure of the peak from the extrapolated baseline, estimated to be ±5 K, and (ii) ε_3, the error arising from a change in specimen emissivity produced by grain growth immediately prior to melting, estimated to be ±10 K. Hence, combining these errors as $\sqrt{(\varepsilon_1^2 + \varepsilon_2^2 + \varepsilon_3^2)}$, we estimate the overall uncertainty in the DTA solidus-temperature measurements to be ±20 K. This is a maximum value, however, and the error in determinations with specimens that showed clear melting-onset temperatures would be somewhat lower. For example, four determinations with as-received Zry gave a mean solidus temperature $\pm 2\sigma$ of 2035 ± 3 K, in excellent agreement with the generally accepted melting temperature of ~2033 K.

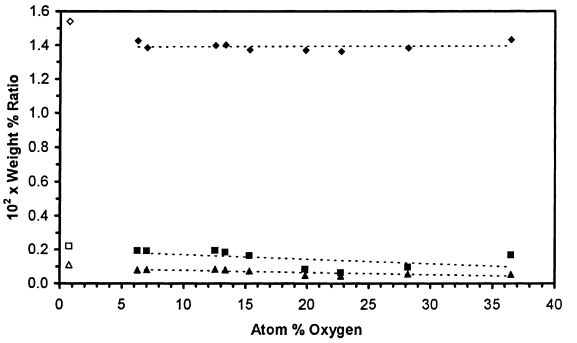

Fig. 4. ICP results (wt% ratios) for Sn/Zr (diamonds), Fe/Zr (squares) and Cr/Zr (triangles) in annealed Zry(O) specimens versus oxygen content. Values for as-received Zircaloy-4 shown as open symbols.

Table 1
Phase content of Zircaloy/oxygen alloys after annealing at 1923 K for 4 h

at.% O	Phase content
6.3	Uniform prior-β Zr (Widmanstätten-structured)
7.0	Uniform prior-β Zr (Widmanstätten-structured)
12.5	α-Zr(O) matrix containing lamellae of prior-β Zr
13.4	α-Zr(O) matrix containing lamellae of prior-β Zr
15.3	α-Zr(O) matrix containing lamellae of prior-β Zr
19.9	Uniform α-Zr(O) matrix
22.7	Uniform α-Zr(O) matrix
28.2	α-Zr(O) matrix containing small isolated region of ZrO_2
36.5	α-Zr(O) matrix containing regions of ZrO_2

Table 2
PDTA results for solidus temperatures

Composition (at.% O)	Solidus (K) ±20 K	Composition (at.% O)	Solidus (K) ±20 K
As-received Zry	2034, 2034		
(0.74)	2037, 2036	Zry/11.2	2188
Zry/2.3	2070	Zry/15.5	2207
Zry/3.7	2072	Zry/17.1	2301
Zry/5.5	2112	Zry/21.0	2327
Zry/8.0	2153	Zry/21.3	2358
Zry/8.7	2169	Zry/25.7	2328
Zry/9.1	2151	Zry/26.9	2337
Zry/9.9	2188	Zry/29.2	2321
Zry/10.2	2207	Zry/32.5	2318
Zry/10.4	2195	Zry/34.4	2318

4. Results

4.1. ICP analyses of annealed Zry(O) alloy specimens

The ICP results are plotted in Fig. 4 as the Sn/Zr, Fe/Zr and Cr/Zr wt% ratios in the specimens versus the nominal O contents. The ratios present in the Zry starting material, calculated from the manufacturer's analysis, are also shown. The results indicate that there was no significant loss of Sn, Fe or Cr during the oxidation/annealing process.

4.2. Optical and SEM examinations of annealed Zry(O) alloy specimens

Polarised-light microscopy on selected specimens identified the phases listed in Table 1. Subsequent SEM/EDX analyses confirmed the phase identifications, and also revealed the presence of small inclusions of a Zr–Sn–O phase at the margins of the ZrO_2 phase in the 28.2 and 36.5 at.% O specimens.

The Zr–O phase diagram [7] predicts formation of the following phases at 1923 K: prior-β-Zr at less than 8 at.% O, coexisting prior-β-Zr and α-Zr in the range 8–17 at.% O, α-Zr in the range 17–29 at.% O, and coexisting α-Zr and ZrO_2 at higher O contents. These predictions are in good agreement with the phases in the annealed specimens, indicating that the Sn, Fe and Cr content of Zry has no major influence on the widths of the various Zr–O phase fields.

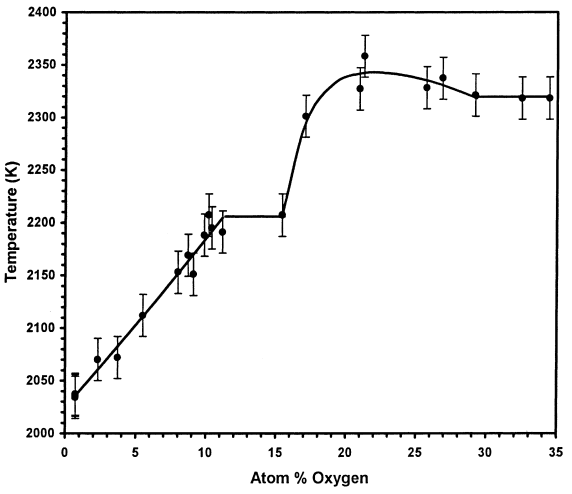

Fig. 5. Plot of solidus temperature versus O-content in Zry(O) alloys. Error bars are ±20 K.

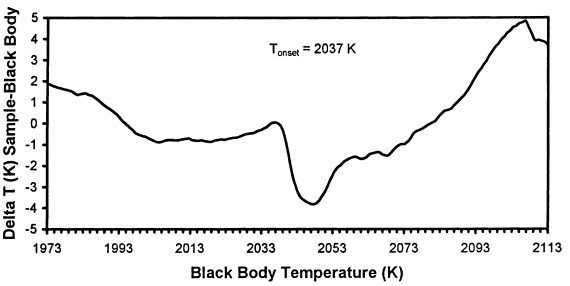

Fig. 6. PDTA trace for as-received Zircaloy-4.

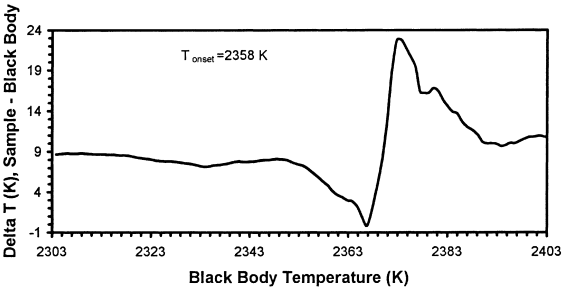

Fig. 7. PDTA trace for Zircaloy/21.3 at.% O specimen.

4.3. PDTA results for melting-onset temperatures

The raw ΔT_{s-bb} and T_{bb} data were each smoothed using a 3-point moving-average procedure to minimise background noise without shifting the peak position. The peak-onset temperatures are listed in Table 2 and plotted against Zry(O) oxygen content in Fig. 5.

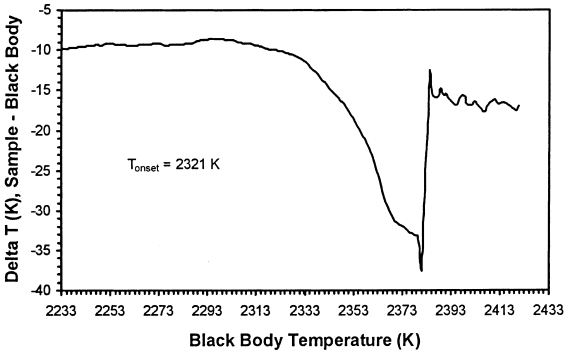

Fig. 8. PDTA trace for Zircaloy/29.2 at.% O specimen.

Figs. 6 and 7 show traces for as-received Zry and for the Zry/21.3 at.% O specimen, respectively, in which the peak-onset temperature is evident from the trace. Fig. 8, the trace for the Zry/29.2 at.% O specimen, is an example of a trace where the point of departure from the baseline is difficult to ascertain precisely. In cases such as this, the parallel observations of specimen melting were used to confirm the peak-onset temperature.

5. Discussion

It is instructive to compare the PDTA results for Zry–O alloys with the data of Ackermann et al. [5], who used direct observation and a pyrometer-based temperature-measurement system to determine the solidus, liquidus and peritectic temperatures for Zr–O alloys. Fig. 9 shows a schematic representation of part of the Zr–O phase diagram, with our results compared with theirs in the accompanying table.

Although there is reasonable agreement in the Zr–O and Zry–O composition ranges for the various reaction

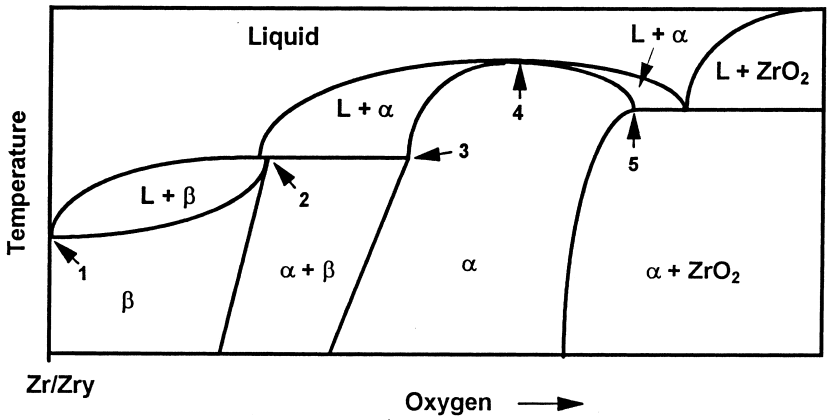

Point	Reaction	Reaction type	Zr-O binary		Zry-O pseudo-binary	
			At.% O	T (K)	At.% O	T (K)
1	β-Zr ↔ L	Melting (Zr) Solidus (Zry)	0	2128	0.74	2035 ± 20
2	β-Zr ↔ L + α-Zr	Peritectic reaction	10.5 ± 0.5	2243 ± 10	~10.5	2203 ± 20
3	α-Zr ↔ L + α-Zr	Peritectic reaction isotherm	19.5 ± 2	2243 ± 10	~15.5	2203 ± 20
4	α-Zr ↔ L	Congruent melting	25 ± 1	2403 ± 10	~22.5	2348 ± 20
5	α-Zr + ZrO_2 ↔ L + α-Zr	Eutectic reaction isotherm	35 ± 1	2338 ± 5	~29.0	2318 ± 20

Fig. 9. Comparison of measured reaction temperatures and compositions with those in the Zr–O system (after Ref. [7]).

types, the solidus temperatures of the Zry–O alloys are somewhat lower than those of the corresponding Zr–O alloys. This difference may be due to the influence of the Zry alloy elements, especially Sn. An alternative explanation, however, may involve the method used in [5], in which ~200 mg samples of pre-oxidised Zr, contained in high density ZrO_2 cups, were repeatedly heated and cooled over the solidus–liquidus temperature range. An insignificant amount of ZrO_2 solution in molten Zr(O) was reported to have occurred during the 10–15 min required for each set of melting/freezing observations. This contention was supported by (i) the good reproducibility of the results (within ±3 K), and (ii) post-test analyses of the Zr(O) samples, using a combustion-based gravimetric method, which gave final O concentrations within 1–2 at.% of the starting compositions (also measured gravimetrically).

The lack of ZrO_2 dissolution is somewhat surprising because subsequent measurements of the dissolution rate of high-density ZrO_2 in molten Zircaloy-4 [11,12] have conclusively shown that rapid ZrO_2 dissolution occurs at or above 2273 K, together with simultaneous O diffusion from oxide to alloy. Thus, it seems reasonable to suggest that the Zr(O) samples used in [5] may have become further oxygenated during each measurement by up to 1–2 at.%, i.e., within the error limits of the analysis method. This uncertainty may be sufficient to account for the different solidus temperatures listed in Fig. 9 for the Zr–O and Zry–O systems, and makes it impossible to definitely attribute any differences in solidus temperatures to the influence of the Zry alloy components (Sn, etc.).

It is beyond the scope of this report to consider the implications of these new results on modelling of fuel-assembly behaviour during a hypothetical SFD accident. The relatively high temperatures of points 4 and 5 in Fig. 9 are of particular note, however. The results indicate that the solidus temperatures for O-saturated Zry quoted in MATPRO [6] and other data compilations are probably 145–185 K too low. We, therefore, recommend a value of 2318 ± 20 K for the solidus temperature of O-saturated cladding in future model revisions.

Acknowledgements

We thank D.G. Evans, A.J. White and C.K. Chow for valuable manuscript reviews and comments, K. Wasney for the ICP measurements and L.C. Brown for the SEM/EDX analyses. Financial support from the CANDU Owners Group, consisting of AECL, Ontario Hydro, Hydro-Quebec and NB Power, is gratefully acknowledged.

References

[1] H. Baker (Ed.), ASM Handbook, vol. 3, Alloy Phase Diagrams, ASM International, Metals Park, OH, 1992.
[2] R.F. Domagala, D.J. McPherson, Trans. AIME 200 (1954) 238.
[3] C. Politis, Report No. KfK-2167, (1975).
[4] A. Skokan, in: Proceedings of the Fifth International Meet on Thermal Nuclear Reactor Safety, KfK-3880/2 (1984) 1035.
[5] R.J. Ackermann, S.P. Garg, E.G. Raugh, J. Am. Ceram. Soc. 60 (1977) 341.
[6] D.T. Hagrman (Ed.), US Nuclear Regulatory Commission Report NUREG/CR-6150, EGG-2720, vol. 4, 1995.
[7] J.P. Abriata, J. Garces, R. Versaci, Bull. Alloy Phase Diagr. 7 (1986) 116.
[8] L.S. Darken, R.W. Gurry, Physical Chemistry of Metals, McGraw-Hill, New York, 1953.
[9] K.T. Conlon, C. Wong, J.W. DeVaal, B.H. McDonald, AECL Proprietary Report, COG-91-270, RC-738, 1994.
[10] P.J. Hayward, I.M. George, J. Nucl. Mater, 265 (1999) 60.
[11] P. Hofmann, Ch. Adelhelm, E. Garcia, M. Markiewicz, J. Burbach, G. Gaussmann, K. Kurz, H. Metzger, Report No. KfK-4200, 1987, pp. 9–27.
[12] P.J. Hayward, I.M. George, J. Nucl. Mater, 265 (1999) 69.